CRYSTAL GROWTH & DESIGN

Article

pubs.acs.org/crystal

Microwave-Assisted Synthesis and Luminescence of Mesoporous RE-Doped YPO_4 (RE = Eu, Ce, Tb, and Ce + Tb) Nanophosphors with Lenticular Shape

Sonia Rodriguez-Liviano,[†] Francisco J. Aparicio,[†] Teresa C. Rojas,[†] Ana B. Hungría,[‡] Lidia E. Chinchilla,[‡] and Manuel Ocaña*,[†]

[†]Instituto de Ciencia de Materiales de Sevilla (CSIC-UNSE), Americo Vespucio 49, Isla de La Cartuja, 41092 Sevilla, Spain

[‡]Departamento de Ciencia de Materiales, Ingeniería Metalúrgica y Química Inorgánica, Facultad de Ciencias, Universidad de Cádiz, 11510 Puerto Real, Cádiz, Spain

W *Web-Enhanced Feature* S *Supporting Information*

ABSTRACT: Mesoporous tetragonal RE:YPO_4 nanophosphors (RE = Eu, Ce, Tb, and Ce + Tb) with a lenticular morphology, narrow size distribution, and high surface area have been prepared by an homogeneous precipitation procedure consisting of aging, at low temperature (80−120 °C) in a microwave oven, ethylene glycol solutions containing only yttrium acetylacetonate and phosphoric acid. This synthesis method involves important advantages such as its simplicity, rapidness (reaction time = 7 min), and high reaction yields. The mechanism of nanoparticle growth has been also addressed finding that the lenticular nanoparticles are formed through an ordered aggregation of smaller entities, which explains their porosity. In all cases, the doping levels were systematically varied in order to optimize the nanophosphors luminescence. All optimum nanophosphors presented a high luminescence quantum yield (QY). In particular, for the Eu and Tb doped systems, the obtained QY values (60% for Eu and 80% for Tb) were the highest so far reported for this kind of nanomaterial. The morphological, microstructural, and luminescent properties of these nanophosphors and their dispersibility in water make them suitable for biomedical applications.

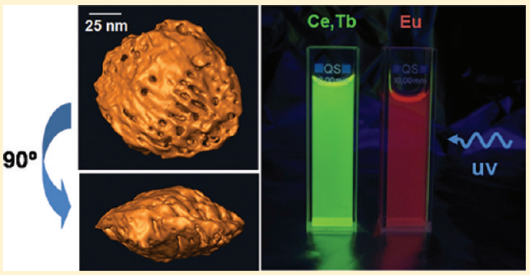

INTRODUCTION

Rare earth (RE) based phosphors have been attracting much attention during the past decade owing to the important advantages that they present when compared with other available luminescent materials (quantum dots or organic dyes), such as low toxicity, photostability, high thermal and chemical stability, high luminescence quantum yield, and sharp emission bands. Among these phosphors, those consisting of a rare earth phosphate ($REPO_4$) (RE = La, Ce, Gd, or Y) matrix doped with RE cations find important applications, especially in optoelectronic (fluorescent lamps,[1] plasma display panels,[2] light emitting diodes,[3] oxygen sensors[4]) and biomedicine (cell labeling,[5] detection of biomolecules,[6] drug delivery[7]). For most of these applications, particles with uniform shape and narrow size distribution are highly desirable. For example, for fluorescent lamps and PDP devices, uniform spherical particles in the sub-micrometer size range are preferred, since they can be more densely packed, which results in a better resolution and brightness.[8] It has been also established that for biosensing, the ideal phosphor must consist of water dispersible nanoparticles with a spherical shape and a high luminescence efficiency,[9] whereas for drug delivery, a high surface area and a mesoporous structure is also required.[7] The availability of uniform phosphors with a different particle size and shape is also required for fundamental studies dealing with the effects of these morphological characteristics on the luminescence efficiency, whose origin still remains unclear.[10]

A large variety of procedures for the synthesis uniform $REPO_4$-based nanophophors with different morphologies and sizes have been recently developed, most of them involving monoclinic $LaPO_4$ as a host matrix. For the RE:YPO_4 system, fewer methods have been reported[10b,11,12] which require, in most cases, high reaction temperatures (180 °C), long aging times (from several hours to days), and the addition of dispersing or capping agents (oleic acid, oleylamine, ethylenediamine tetraacetic acid, sodium dodecyl sulfate, citrate, glycerol).

In this paper, we report a very simple and fast (7 min) procedure for the synthesis of mesoporous tetragonal RE:YPO_4 nanophosphors with a lenticular morphology, narrow size distribution, and high surface area, which are suitable for biomedical applications. This method is based on a homogeneous precipitation process conducted at rather low temperature (80−120 °C) in ethylene glycol (EG) solutions containing only phosphoric acid (H_3PO_4) and RE acethylacetonate ($RE(acac)_3$). It should be noted that mesoporous

Received: June 27, 2011
Revised: November 4, 2011
Published: December 5, 2011

RE:YPO_4 structures have been previously prepared only by Luo et al. who used a commercial mesoporous silica template, which was further removed by HF treatment, resulting in mesoporous particles with irregular morphology and size.[7c]

Different doping cations were selected to cover a broad range of the visible spectrum: Eu^{3+} (red emitting), Tb^{3+} (green emitting), and Ce^{3+} (blue emitting). It should be noted that whereas the Eu and Tb systems have been previously addressed, this is the first report dealing with the structural (CE solubility limit) and luminescent properties of Ce:YPO_4 nanophosphors. We also extended our synthesis procedure to the synthesis of Ce,Tb:YPO_4 nanoparticles for the first time in this system aiming to increase, through a well-known energy transfer process,[1,2] the Tb^{3+} green luminescence, which is usually weak since the electronic transitions within the $4f^n$ configuration of Tb^{3+} are strongly forbidden. In all cases, the doping levels were systematically varied in order to obtain nanophosphors with optimized luminescent properties.

■ EXPERIMENTAL SECTION

Reagents. Yttrium(III) acetylacetonate hydrate ($Y(C_5H_7O_2)_3{\cdot}xH_2O$, Alfa Aesar, 99.9%), cerium(III) acetylacetonate hydrate ($Ce(C_5H_7O_2)_3{\cdot}xH_2O$, Aldrich), europium acetylacetonate hydrate ($Eu(C_5H_7O_2)_3{\cdot}xH_2O$, Alfa Aesar, 99.9%), terbium acetylacetonate hydrate ($Tb(C_5H_7O_2)_3{\cdot}xH_2O$, Alfa Aesar, 99.9%), orthophosphoric acid (H_3PO_4, Aldrich, 85%), and ethylene glycol (EG, Fluka, <99.5%) were used as received.

Synthesis of Samples. The typical procedure for the synthesis of the YPO_4 samples was as follows. Weighted amounts of $Y(acac)_3$ were dissolved in EG under magnetic stirring while heating at low temperature (~75 °C) to favor dissolution. Then, these solutions were cooled to room temperature and the desired amount of phosphoric acid was admixed. After homogenization, the final solutions (total volume = 10 cm^3) placed in tightly closed reactors were heated from room temperature to the target value in a microwave oven (Sineo MDS-8), using a heating rate of 14 °C min^{-1}. After the desired temperature was reached, the solutions were aged up to 1 h, unless otherwise specified. For comparison, some experiments were also carried out using a conventional oven for heating. The resulting dispersions were cooled down to room temperature, centrifuged to remove the supernatants, and washed twice with ethanol and once with double distilled water. Finally, the precipitates were dispersed in water. For some analyses, the powders were dried at room temperature.

For the synthesis of the RE-doped YPO_4 phosphors, we proceeded as described above for the case of undoped YPO_4 but incorporating the desired amount of the doping cation precursor to the starting $Y(acac)_3$ solution.

Characterization. Particle shape was examined by transmission (TEM, Philips 200CM) electron microscopy. Particle size distributions were obtained by counting several hundreds of particles from the TEM micrographs, and by dynamic light scattering (DLS, Malvern, Zetamaster) using water dispersions. High angle annular dark field (HAADF) scanning transmission electron microscopy (STEM) tomography studies[13] were also performed to characterize the three-dimensional morphology of the particles and their porosity. The HAADF-STEM images were acquired on a JEOL 2010 field emission gun transmission electron microscope operated at 200 kV. For the tomography studies, a single tilt series of HAADF-STEM images was recorded over a wide angular range (from −68° to +70°) every 2° using a Fischione Ultra-Narrow Gap tomography holder. Images were aligned sequentially using Inspect 3D. Reconstructions were performed with Inspect 3D using an iterative routine (SIRT), which constrains the reconstructed volume to best match the original images when reprojected back along the original tilt directions. Voxel projections and surface rendering (after a segmentation process when needed) were undertaken using Amira software.

The quantitative composition of the samples was analyzed by inductively coupled plasma atomic emission spectroscopy (ICP-AES, Horiba Jobin Yvon, Ultima 2). The crystalline structure of the prepared samples was assessed by X-ray diffraction (XRD, Panalytical, X'Pert Pro). Unit cell parameters were determined from the XRD data (collected at intervals of 0.03° (2θ) for an accumulation time for interval of 10 s) by Rietveld refinement using the X'Pert HighScore Plus software. The starting parameters were taken from Ni et al.[14] To gain additional information on the structural features of the synthesized nanoparticles, they were also characterized by high resolution transmission electron microscopy (HRTEM, Philips 200CM). The digital diffraction patterns (DDP) were obtained from the HRTEM images using Digital Micrograph software.[15]

The infrared spectra (FTIR) of the nanophosphors diluted in KBr pellets were recorded in a Jasco FT/IR-6200 Fourier transform spectrometer. Thermogravimetric analyses (TGA) were performed in air at a heating rate of 10 °C min^{-1}, using a Q600 TA Instrument. BET specific surface area was measured in a Micromeritics ASAP 2010 apparatus with nitrogen at 77 K. Before measurements, the samples were heated under vacuum at 150 °C for 2 h.

The excitation and emission spectra of the samples dispersed in water (0.5 mg cm^{-3}) were recorded in a Horiba Jobin-Yvon Fluorolog3 spectrofluorometer operating in the front face mode. The photoluminescence quantum yield (QY), defined as the ratio between photons emitted and absorbed by the suspensions, was determined by an absolute method. The used set up consisted of an integrating sphere (Labsphere) with its inner face coated with Spectralon, attached to the spectrofluorometer.[16] A nonfluorescent sample consisting of undoped YPO_4 nanoparticles having morphological characteristics similar to those of the analyzed RE:YPO_4 sample was used in all cases to mimic the scattering properties of the latter. Spectral correction curves for sphere and emission detector were provided by Horiba Jobin-Yvon. Lifetime measurements were obtained under pulsed excitation at 532 nm by using the second harmonic of a Nd:YAG laser (Spectra Physics model DCR 2/2A 3378) with a pulse width of 10 ns and a repetition rate of 10 Hz. The fluorescence was analyzed through an ARC monochromator model SpectraPro 500-i and then detected synchronously with an EMI-9558QB photomultiplier and recorded by a Tektronix TDS420 digital oscilloscope.

The CIE color coordinates were calculated from the emission spectra considering a 2° observer. The photographs showing the luminescence of the nanophosphors either in powdered form deposited on Millipore filters or in water dispersions were taken under illumination with ultraviolet radiation (λ = 254 nm) filtered from a Hg discharge lamp.

■ RESULTS AND DISCUSSION

Synthesis and Characterization of Undoped YPO_4 Nanoparticles. It has been well documented that the formation of uniform particles by precipitation in solution requires a homogeneous process, which can be achieved, for example, through a slow and controlled release of the precipitating anions or cations in the reaction medium.[17] We selected the latter strategy using $RE(acac)_3$ as precursors, which in solution, can be decomposed on heating, thus liberating the RE^{3+} cations.[18] If phosphate anions are present in these solutions, this decomposition process drives the precipitation of $REPO_4$. EG was selected as the solvent because such RE precursors are not water-soluble and mainly because polyols have been amply shown to be suitable solvents for the synthesis of nanomaterials, since they may act not only as solvent but also as complexing and/or capping agent, thus limiting particle growth.[19] Finally, we used a microwave oven for heating because it has been shown that this heating source usually involves much shorter reaction times and higher reaction yields than those involved in a conventional heating procedure.[20]

According to the classic theory of precipitation developed by LaMer and Dinegar,[21] it is well-known that another requisite for the precipitation of uniform particles is the separation of the nucleation and growth processes, which only occurs under a precise set of experimental conditions (reagents concentration, temperature, and aging time).[17] To establish such conditions, we performed a systematic study of the effects of the experimental parameters on the morphological characteristics of the precipitates, first addressing the undoped YPO_4 system, for simplicity.

We found that the aging of 0.02 mol dm^{-3} $Y(acac)_3$ and 0.15 mol dm^{-3} H_3PO_4 solutions in EG at 120 °C using the microwave oven resulted in the nanoparticles shown in Figure 1, which as indicated by XRD (Figure 2) consisted of tetragonal YPO_4 (JCPDS No 1-84-335). It would seem from the TEM picture that this sample is composed by a mixture of spherical and elongated particles. However, the higher contrast of the elongated particles suggests a homogeneous lenticular morphology so that the apparently spherical particles are in fact oblate spheroids lying with their shorter axis normal to the TEM grid plane, whereas those apparently elongated laid with their shorter axis almost parallel to such a plane. This suggestion was confirmed by the electron tomography experiment which permits to reconstruct the 3D shape of the object and gives an unique information of the inside of the reconstructed nanoparticle. Thus, the surface rendered representations of the segmented reconstructed volume of a single nanoparticle at two different projections shown in Figure 3 (up) evidenced unambiguously the lenticular shape of the nanoparticles. In this figure, a very rough surface and some pores are also observed. When cutting the reconstructed volume with a slice using Amira program (Figure 3, down), an internal mesoporous structure with a pore diameter of ca. 4 nm, became also clear. A movie (in mpg format) showing the full dynamic tomogram is available as a web enhanced object. In agreement with such internal porosity, the BET surface area measured for this sample was much higher (145 m^2 g^{-1}) than that calculated (~14 m^2 g^{-1}) assuming smooth spheres of tetragonal YPO_4 (density = 4.28 g cm^{-3}).

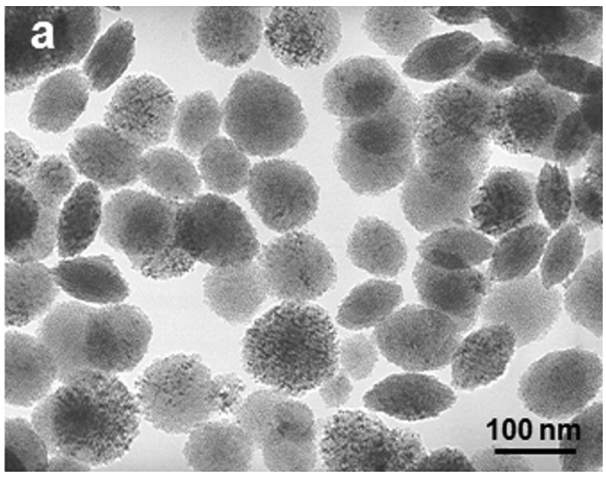

Figure 1. TEM micrograph of the YPO_4 sample obtained by aging at 120 °C for 60 min, a 0.02 mol dm^{-3} $Y(acac)_3$ and 0.15 mol dm^{-3} H_3PO_4 solution in ethylene glycol.

These YPO_4 nanoparticles were also free of organic contamination as clearly indicated by FTIR spectroscopy. Thus, their IR absorption spectrum (Figure 4) only displayed several bands at <1300 cm^{-1}, corresponding to vibrations associated with the phosphate groups,[11c] along with a weaker absorption at 1640 cm^{-1} due to the bending vibrations of adsorbed water and a very broad feature at about 3415 cm^{-1} mainly attributable to the stretching O−H vibration of the water molecules.[22] Nevertheless, the possible contribution to the latter band of OH^- anions of different origin cannot be neglected.[22] In fact, the TGA curve measured for this sample (Figure S1, Supporting Information) showed a 6% weight loss in the 25−200 °C range, due to the release of absorbed water,

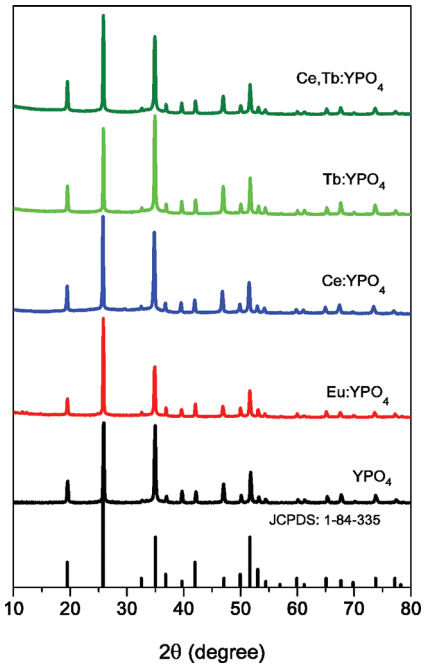

Figure 2. X-ray diffraction patterns obtained for the YPO_4 sample shown in Figure 1 and for the $Eu_{0.25}Y_{0.75}PO_4$, $Ce_{0.1}Y_{0.9}PO_4$, $Tb_{0.2}Y_{0.8}PO_4$, and $Ce_{0.05}Tb_{0.05}Y_{0.9}PO_4$ samples prepared as described in Table 2.

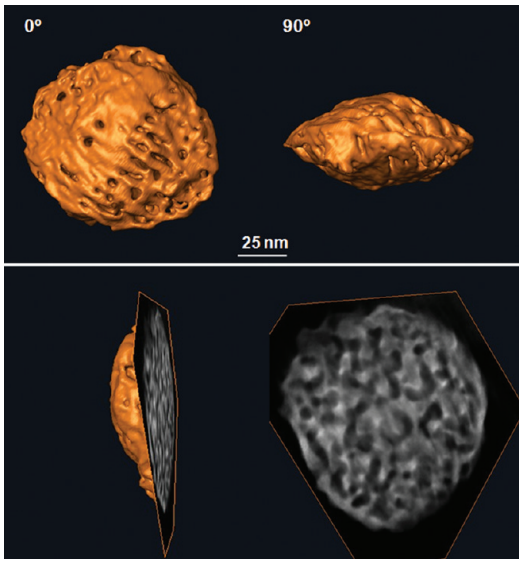

Figure 3. Surface rendered representations of the segmented reconstructed volume of a single nanoparticle at two different projections (up) and transverse slice from the reconstructed tomogram (down).

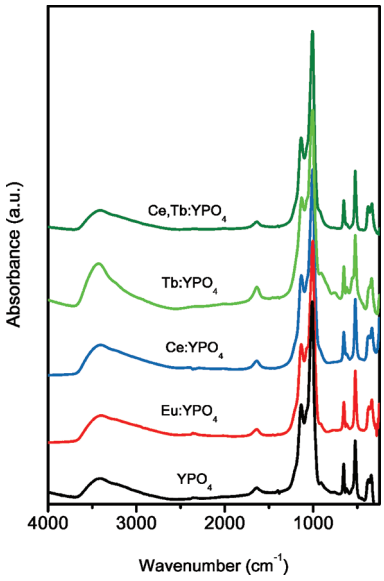

Figure 4. Infrared spectrum obtained for the YPO_4 sample shown in Figure 1 and for the $Eu_{0.25}Y_{0.75}PO_4$, $Ce_{0.1}Y_{0.9}PO_4$, $Tb_{0.2}Y_{0.8}PO_4$, and $Ce_{0.05}Tb_{0.05}Y_{0.9}PO_4$ samples prepared as described in Table 2.

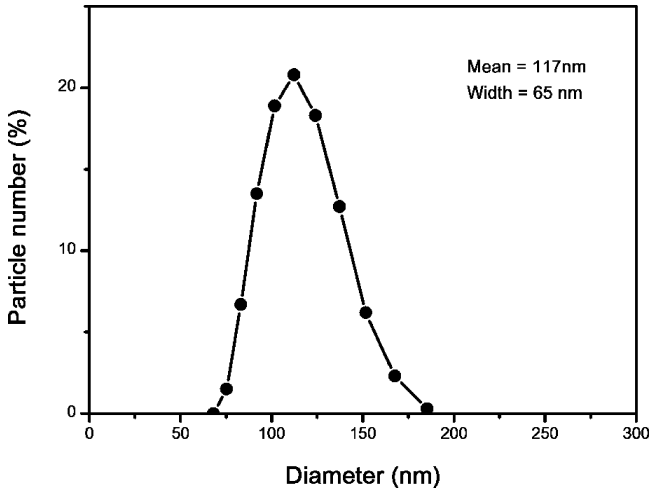

Figure 5. Particle size distribution obtained by DLS for the YPO_4 sample shown in Figure 1.

followed by a similar (5.6%) loss between 200 and 800 °C, which might be associated to such OH groups.

The mean diameter of the particles estimated from the TEM images was 115 ± 17 nm, whereas their mean thickness was 48 ± 13 nm (axial ratio ~ 2.4) (Table 1). It should be noted that this thickness was obtained from the particles with ellipsoidal appearance assuming that they laid with the shorter axis completely parallel to the grid surface. Therefore, the given value is rather approximated and likely higher than the real thickness. Particle size distribution evaluated for aqueous dispersions of this sample by DLS (Figure 5) resulted in a mean particle diameter (117 ± 65 nm) very similar to the longest particle dimension obtained from the TEM micrographs (115 ± 17 nm), which manifested the absence of agglomerates and therefore the good dispersibility of the YPO_4 nanoparticles in water.

The reagents concentrations were found to be a key factor determining the size of the lenticular nanoparticles. Thus, when the yttrium precursor concentration was raised from 0.001 to 0.06 mol dm^{-3} (solubility limit of $Y(acac)_3$ in EG), keeping constants the other experimental conditions, the mean diameter of the lenticular particles decreased from 227 ± 27 to 92 ± 14 nm, in spite of the observed enhancement of the reaction yield from 75 to 90% as increasing the $Y(acac)_3$ concentration (Table 1).

Such high values of the reaction yield, which are associated with the use of microwave-assisted heating,[20] are an additional advantage of the synthesis procedure developed in this work. Particle size could be also tailored by varying the amount of H_3PO_4 added to the starting solutions. Thus, for a $Y(acac)_3$ concentration of 0.005 mol dm^{-3}, an increase of the mean diameter from 66 ± 8 to 161 ± 24 nm resulted when the phosphoric acid concentration was raised from 0.05 to 0.25 mol dm^{-3} (Table 1). At much higher H_3PO_4 concentrations (1 mol dm^{-3}), agglomerates consisting of irregular particles were detected, whereas at ≤0.01 mol dm^{-3}, only a slight turbidity was observed due to a gel-like precipitate. The aging temperature (in the range 80−150 °C) did not have an important effect on the morphological characteristics of the nanoparticles (Table 1). However, the heating mode was found to be a key factor for the preparation of uniform dispersions. Thus, heating the above solutions for 1 h in a conventional oven yielded ill-defined precipitates that did not evolve to uniform particles even after a prolonged aging up to 24 h (Figure S2, Supporting Information).

To explain the above-described effects of the different experimental parameters on the morphological characteristics

Table 1. Morphological Characteristics of the Particles Precipitated after Aging, at Different Temperatures for 60 min, EG Solutions Containing Different Concentrations of $Y(acac)_3$ and H_3PO_4[a]

$[Y(acac)_3]$ mol·dm^{-3}	$[H_3PO_4]$ mol·dm^{-3}	temperature °C	shape	diameter nm	thickness nm	axial ratio	reaction yield %
0.060	0.15	120	lenticular	92 ± 14	56 ± 13	1.6	90
0.020	0.15	120	lenticular	115 ± 17	48 ± 13	2.4	74
0.005	0.15	120	lenticular	134 ± 17	52 ± 17	2.6	77
0.001	0.15	120	lenticular	227 ± 37	117 ± 17	1.9	75
0.005	0.01	120	gel-like				
0.005	0.05	120	lenticular	66 ± 8	33 ± 3	2.0	48
0.005	0.25	120	lenticular	161 ± 24	54 ± 21	3.0	87
0.005	1.00	120	irregular				
0.005	0.15	80	lenticular	139 ± 19	62 ± 15	2.2	77
0.005	0.15	150	lenticular	129 ± 16	44 ± 11	2.9	70

[a]The reaction yield is also included.

of the precipitated particles, their mechanism of formation was investigated.

Growth Mechanism of the YPO_4 Nanoparticles. The rough surface and mesoporosity of the lenticular YPO_4 nanoparticles (Figure 3) seem to indicate that they were formed through an ordered aggregation of smaller subunits (primary particles), as it has been previously reported for many other colloidal systems.[23] Such an aggregation process is energetically favored because the formation of larger entities greatly reduces the interfacial energy of the small primary particles.

The HRTEM micrograph taken from a single particle lying with the longest dimension parallel to the grid plane and the DDP spots obtained from this HRTEM image (Figure 6a), supported such suggestion and gave additional information on the structural features of the lenticular nanoparticles. Thus, the HRTEM picture clearly shows the presence of several crystalline domains within the particle with a small misorientation deviating from the perfect alignment between crystallites. In agreement with this observation, the DDP obtained for this area of the nanoparticle showed elongated spots, which corresponded to an interplanar distance of 3.4 Å.

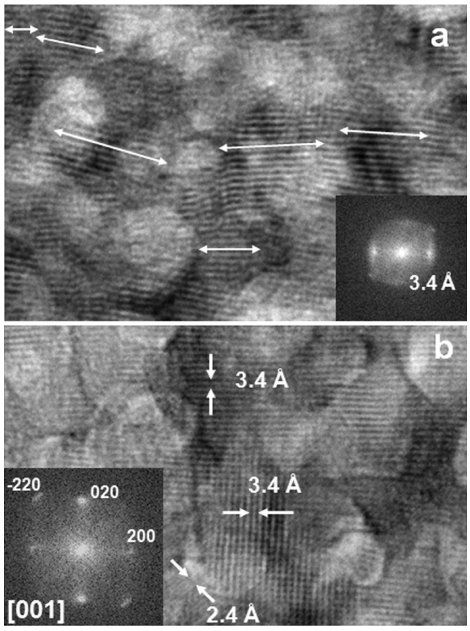

Figure 6. HRTEM images and DDP patterns for the YPO_4 sample shown in Figure 1, showing its polycrystalline character (a) and a single crystalline domain (b).

The orientation of the crystallographic axes of the tetragonal YPO_4 structure in the building units could be determined from HRTEM and the DDP spots obtained for the single domain (Figure 6b). Thus, two sets of perpendicular planes with an interplanar distance of 3.4 Å are clearly observed in the HRTEM image, which correspond to the 020 and 200 planes of the tetragonal YPO_4 phase (JCPDS No 1-84-335), indicating that the crystallographic *c* axis was perpendicular to the shorter dimension of the lenticular nanoparticle. Consequently, the whole set of spots observed in the DDP corresponded to the [001] zone axis of such structure. This finding indicates that the primary particles preferentially attach through theirs crystalline faces parallel to the *c* axis. Such directional aggregation has been previously observed for some other colloidal systems, usually being attributed to a preferential adsorption of ligands on specific crystal faces, which only leaves the clean faces available for attachment.[23c] In our case, the only species with complexing ability are those resulting from the decomposition of the acetylacetonate precursor and EG, which were not present in the final nanoparticles (Figure 5). However, they could have been weakly adsorbed on the surface of the initially formed primary particles and desorbed during the aggregation process, as suggested for other systems.[23c]

Aiming to observe how the aggregation process proceeded, we examined the precipitates after different aging times. However, it was found that after 7 min (time required to reach 120 °C at the selected heating rate), the lenticular nanoparticles were already formed, with a size similar to the final value (Figure S3, Supporting Information) indicating that nanoparticles formation was extremely fast, which is another of the most important advantages of the herein reported microwave-assisted synthesis method. This reaction rapidness would explain the effects of the heating method on the morphology of the precipitated particles. Thus, at such a high reaction kinetic, the solutions heating rate becomes an essential factor, since a rapid heating, as that associated with microwave irradiation,[20] would favor a single nucleation event and therefore the formation of uniform particles, whereas a slower heating rate, as that involved in a conventional heating, would give a chance for heterogeneous nucleation. To observe intermediate precipitation products, we had to decrease the aging time to 2 min when the temperature reached in the solution was 57 °C, finding that, even at this low temperature and short aging time, the precipitate already contained some lenticular particles of about 100 nm along with tiny and irregular entities (Figure S3, Supporting Information), which could be considered as the primary particles. This formation mechanism is summarized in Figure 7.

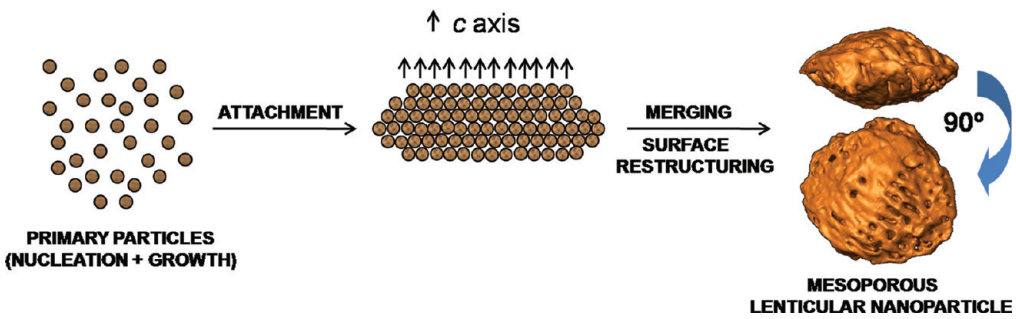

Figure 7. Schematic diagram of the mechanism of formation of the lenticular YPO_4 mesoporous nanoparticles.

Table 2. Nominal (nom) and Experimental (ICP) Y/RE, Eu/RE, Tb/RE, and Ce/RE (RE = Y + Eu + Tb + Ce) mol Ratios (%) of the RE-Doped YPO_4 Lenticular Nanoparticles

sample	Y/RE Nom.	Y/RE ICP	Eu/RE Nom.	Eu/RE ICP	Tb/RE Nom.	Tb/RE ICP	Ce/RE Nom.	Ce/RE ICP
$Eu_{0.05}Y_{0.95}PO_4$	95	95.9	5	4.1				
$Eu_{0.10}Y_{0.90}PO_4$	90	91.4	10	8.6				
$Eu_{0.15}Y_{0.85}PO_4$	85	86.5	15	13.5				
$Eu_{0.25}Y_{0.75}PO_4$	75	76.8	25	23.2				
$Tb_{0.05}Y_{0.95}PO_4$	95	95.6			5	4.4		
$Tb_{0.10}Y_{0.90}PO_4$	90	90.1			10	9.9		
$Tb_{0.15}Y_{0.85}PO_4$	85	84.7			15	15.3		
$Tb_{0.20}Y_{0.80}PO_4$	80	80.4			20	19.6		
$Ce_{0.05}Y_{0.95}PO_4$	95	94.9					5	5.1
$Ce_{0.10}Y_{0.90}PO_4$	90	90.6					10	9.3
$Ce_{0.15}Y_{0.85}PO_4$	85	85.4					15	14.5
$Ce_{0.05}Tb_{0.05}\ Y_{0.90}PO_4$	90	90.2			5	4.6	5	5.1
$Ce_{0.10}Tb_{0.05}\ Y_{0.85}PO_4$	85	85.7			5	4.4	10	9.9

The variations in particle size observed when varying the concentration of reagents can be now explained, at least qualitatively. It is obvious that the main factor determining an aggregation process of colloidal entities is the balance between attractive and repulsive forces. However, the reasons explaining the ordered aggregation into uniform particles of a given size are not so clear. Recently, Privman et al.[23b] developed a theoretical model, which is able to reproduce the size of the secondary particles grown by aggregation when applied to several test systems (gold or cadmium sulphide spheres). This model involves several parameters such as supersaturation, surface tension, and diffusion coefficient of solutes, which determine the rate of primary particles generation and the number of subunits per secondary particle. These authors found that as the rate of primary particles generation increased, the final particles were smaller, which is in agreement with the decrease of particle diameter observed for our system as increasing the yttrium precursor concentration since, according to the theory of LaMer and Dinegar,[21] the highest the Y^{3+} concentration, the highest the precipitation rate of primary particles. Following the same reasoning, the particle size should also increase by decreasing the phosphate concentration. However, particle size decreased when the H_3PO_4 concentration was lowered from 0.25 to 0.01 mol dm^{-3} (Table 1), which could be due to the noticeable decrease of the precipitation yield (from 87 to 48%) occurring when lowering the H_3PO_4 concentration (Table 1).

Synthesis and Characterization of RE-Doped YPO_4 Nanophosphors. As shown in Table 2, for all doped samples, the doping level was varied within a wide range to optimize the emission properties of the nanophosphors. In the case of the Ce, Tb codoped system, we kept constant the Tb content (Tb/Y + Ce + Tb mol ratio = 5%) and varied the amount of Ce. Table 2 also shows a rather good agreement between the nominal and experimental composition of all samples, which indicates that the kinetics of precipitation of all doping cations was similar to that of Y^{3+}.

It is important to mention that for the Eu or Tb systems, uniform nanoparticles with shape (Figure S4, Supporting Information), size (Table 3), and crystalline structure (Figure 2) similar to those of the undoped YPO_4 sample were obtained if the RE/Y + RE mol ratio was kept ≤25%. At a higher value of this magnitude (35%), a mixture of lenticular nanoparticles and nanowires was detected (Figure S4, Supporting Information). Such heterogeneous samples were discarded for further studies.

Table 3. Particle Size of the RE-Doped YPO_4 Lenticular Nanoparticles Measured from the TEM Micrographs and by DLS

sample	diameter nm	thickness nm	diameter (DLS) nm
$Eu_{0.05}Y_{0.95}PO_4$	123 ± 15	46 ± 10	
$Eu_{0.10}Y_{0.90}PO_4$	125 ± 19	67 ± 8	
$Eu_{0.15}Y_{0.85}PO_4$	119 ± 21	42 ± 13	
$Eu_{0.25}Y_{0.75}PO_4$	129 ± 24	53 ± 22	123 ± 38
$Tb_{0.05}Y_{0.95}PO_4$	110 ± 20	46 ± 17	
$Tb_{0.10}Y_{0.90}PO_4$	117 ± 17	49 ± 5	
$Tb_{0.15}Y_{0.85}PO_4$	113 ± 23	56 ± 9	
$Tb_{0.20}Y_{0.80}PO_4$	115 ± 21	53 ± 16	114 ± 28
$Ce_{0.05}Y_{0.95}PO_4$	117 ± 18	48 ± 10	
$Ce_{0.10}Y_{0.90}PO_4$	125 ± 14	50 ± 7	120 ± 34
$Ce_{0.15}Y_{0.85}PO_4$	146 ± 24	64 ± 17	
$Ce_{0.05}Tb_{0.05}\ Y_{0.90}PO_4$	121 ± 18	58 ± 10	133 ± 38
$Ce_{0.10}Tb_{0.05}\ Y_{0.85}PO_4$	128 ± 19	72 ± 14	

For the Ce:YPO_4 system, the incorporation of a Ce amount ≤ 10% to the YPO_4 nanoparticles had no significant effects on their shape (Figure S4, Supporting Information), size (Table 3), and crystalline structure (Figure 2). However, for a 15% Ce content, the XRD pattern (Figure S5, Supporting Information) of the resulting lenticular (Table 3) nanoparticles revealed the presence of a weak reflection corresponding to monoclinic $CePO_4$ (JCPDS No. 32-199) in addition to those of the tetragonal phase, suggesting that the Ce^{3+} solubility limit in tetragonal YPO_4 is <15% (Ce/Y + Ce mol ratio). Such an additional $CePO_4$ reflection was more evident for a sample containing a higher amount of cerium (20%), which consisted of a mixture of lenticular nanoparticles and bigger ellipsoidal particles (Figure S4, Supporting Information), the latter probably corresponding to the monoclinic phase.

A similar behavior was observed for the Ce,Tb codoped YPO_4 samples; that is, uniform lenticular (Figure S4, Supporting Information) nanoparticles (Table 3) having tetragonal structure (Figure 2) were obtained for a Ce content ≤10%. For higher doping levels (15%), a mixture of ellipsoidal and lenticular particles (Figure S4, Supporting Information) was detected whose XRD pattern also showed a mixture of tetragonal and monoclinic phases (Figure S7, Supporting Information).

The comparison of the unit cell parameters measured for the doped samples with those of the undoped nanoparticles (Table

Table 4. Unit Cell Parameters and Unit Cell Volume Measured for the RE-Doped YPO_4 Lenticular Nanoparticles

sample	$a = b$ (Å)	c (Å)	V (Å^3)
blank (YPO_4)	6.8804(2)	6.0427(2)	286.0586
$Eu_{0.05}Y_{0.95}PO_4$	6.8861(4)	6.0449(5)	286.6395
$Eu_{0.15}Y_{0.85}PO_4$	6.8952(3)	6.0552(4)	287.8898
$Eu_{0.25}Y_{0.75}PO_4$	6.9084(3)	6.0634(4)	289.3818
$Tb_{0.05}Y_{0.95}PO_4$	6.8832(6)	6.0431(8)	286.3144
$Tb_{0.15}Y_{0.85}PO_4$	6.8869(5)	6.0477(7)	286.8426
$Tb_{0.20}Y_{0.80}PO_4$	6.8946(6)	6.0521(7)	287.6918
$Ce_{0.05}Y_{0.95}PO_4$	6.8914(4)	6.0492(6)	287.2906
$Ce_{0.10}Y_{0.90}PO_4$	6.9029(4)	6.0548(5)	288.5113
$Ce_{0.05}Tb_{0.05}Y_{0.90}PO_4$	6.8924(5)	6.0485(6)	287.3325
$Ce_{0.10}Tb_{0.05}\ Y_{0.85}PO_4$	6.9027(4)	6.0592(6)	288.7013

4) clearly demonstrated the incorporation of the RE cations into the tetragonal YPO_4 lattice, since a progressive unit cell expansion was detected as increasing the doping level, in agreement with the highest ionic radius of Ce^{3+} (1.14 Å), Eu^{3+} (1.07 Å), and Tb^{3+} (1.04 Å) when compared to that of Y^{3+} (1.015 Å).[24]

The nanophosphors particles could be also well dispersed in water, as indicated by the similitude between the values of particle size resulting from DLS measurements (Figure S6, Supporting Information) and those obtained from the TEM micrographs (Table 3). In addition, they were not contaminated by organic species, as shown by their FTIR spectrum (Figure 4) and presented a high BET surface area (for example, 84 m^2 g^{-1}, for the $Eu_{0.25}Y_{0.75}PO_4$ sample).

Luminescent Properties. The emission spectra recorded for the as-synthesized Eu:YPO_4 nanophosphors using an excitation wavelength of 395 nm (direct excitation of the Eu^{3+} ground state to a higher level of the 4f-manifold ($^7F_0$-$^5L_6$)[7c]) are shown in Figure 8.

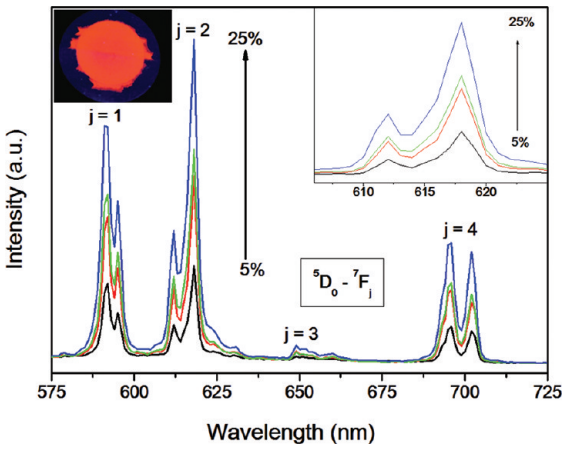

Figure 8. Emission spectra (λ_{ex} = 395 nm) obtained for Eu:YPO_4 nanophosphors having different doping levels (5, 10, 15, 25%). Insets: enlarged view of the spectra showing the most intense emissions (right) and photograph of the $Eu_{0.25}Y_{0.75}PO_4$, phosphor deposited on a Millipore filter, under UV (λ = 254 nm) irradiation (left).

As observed, all spectra displayed the emission bands due to the $^5D_0$-^7F_J (J = 1, 2, 3, and 4) electronic transitions expected for the Eu^{3+}cations in the tetragonal YPO_4 matrix,[7c,10b] having the most intense emissions in the 580−620 nm region, which are responsible for the strong orange-red luminescence (color coordinates: x = 0.624, y = 0.373) (Figure S8, Supporting Information) observed for this sample (Figure 8, left inset and Figure S9, Supporting Information). It is important to mention that the relative intensity of the $^5D_0$-$^7F_2$ emission band was higher than that associated with the $^5D_0$-$^7F_1$ transition, which is expected for Eu^{3+} cations located in crystallographic sites without an inversion center, as is the case for the Y^{3+} site (D_{2d} symmetry) in the YPO_4 tetragonal structure.[10a] It must be also noticed that in previous works conducted with Eu-doped YPO_4 nanowires[22] and mesoporous Eu:YPO_4 samples,[7c] the maximum emission intensity was observed for an Eu content between 5 and 7% since at higher doping levels, a decrease of the emission intensity was detected as a consequence of the concentration quenching effect.[22] However, in our case, the intensity of the emission bands increased by increasing the Eu doping level within the whole studied Eu concentration range (5−25%). Nevertheless, the values of the fluorescence quantum yield (QY) included in Table 5 also suggested the presence of a

Table 5. Quantum Yield of the Lenticular RE-Doped YPO_4 Nanophosphors Having Different Doping Levels[a]

sample	QY (%)
$Eu_{0.05}Y_{0.95}PO_4$	62.9
$Eu_{0.10}Y_{0.90}PO_4$	61.1
$Eu_{0.15}Y_{0.85}PO_4$	54.9
$Eu_{0.25}Y_{0.75}PO_4$	48.8
$Tb_{0.05}Y_{0.95}PO_4$	80.7
$Tb_{0.10}Y_{0.90}PO_4$	66.6
$Tb_{0.15}Y_{0.85}PO_4$	44.8
$Ce_{0.05}Tb_{0.05}\ Y_{0.90}PO_4$	29.5

[a]Excitation wavelengths: 395 nm for the Eu system, 351 for the Tb system, and 320 nm for the Ce−Tb system.

certain concentration quenching process in our samples, since they progressively decreased from 62.9 to 48.8% when the Eu content was increased up to 25%.

To confirm such a suggestion, lifetimes of $^5D_0$ Eu manifold have been measured under the excitation provided by the second harmonic of a pulsed Nd:YAG laser (λ_{exc} = 532 nm). This excitation efficiently populates the $^5D_1$ multiplet ($^7F_0 \rightarrow {}^5D_1$ transition) which then populates the $^5D_0$ state via nonradiative relaxation,[10a] from where the different visible emissions originate. It has been verified that the emission spectra under this excitation are coincident with those obtained after 395 nm excitation shown in Figure 8. The normalized temporal decays of the $^5D_0$ level, measured at λ_{em} = 618 nm ($^5D_0 \rightarrow {}^7F_2$ transition), for different Eu concentrations are shown in Figure 9. The emission lifetimes have been evaluated from these measurements as[25]

$$\tau = \int_0^\infty tI(t)\,dt \Big/ \int_0^\infty I(t)\,dt$$

It can be observed that there is a monotonous decrease in the emission lifetime which varies from τ = (3.3 ± 0.2) ms to τ = (1.8 ± 0.1) ms when europium concentration is increased from 5% to 25% respectively, as is depicted in the inset of Figure 9. It also has been checked that the same values are obtained when the decays are measured in the other luminescence bands originated from the $^5D_0$ Eu level. Consequently, it can be concluded that concentration quenching is present in our samples for doping levels above 5%, in agreement with the QY values discussed above.

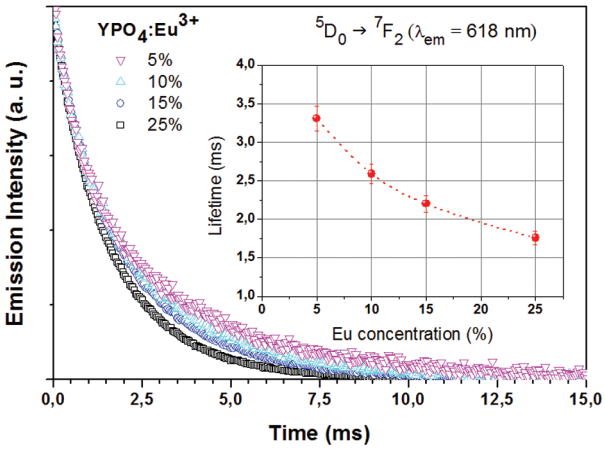

Figure 9. Decay curves obtained for the $^5D_0 \rightarrow {}^7F_2$ transition in the Eu:YPO_4 samples having different Eu content, after excitation at 532 nm ($^5D_1$ level). Inset: evolution of the lifetimes with Eu content.

Therefore, the most efficient Eu:YPO_4 nanophosphor is that containing a 5% of Eu (mole ratio). It is important to notice that the QY of this sample is higher (~60%) than the highest value ever reported for Eu:YPO_4 nanoparticles (40%).[11b]

Additional information on the luminescent properties of the Eu-doped nanophophors was obtained from the excitation spectrum recorded by monitoring the most intense Eu^{3+} emission (618 nm), which is illustrated for the case of sample $Eu_{0.05}Y_{0.95}PO_4$ (Figure 10).

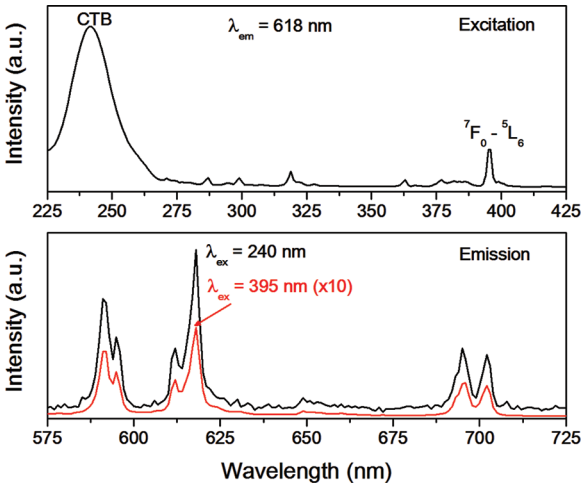

Figure 10. Excitation (top) and emission (bottom) spectra obtained for the $Eu_{0.25}Y_{0.75}PO_4$ nanophosphor.

This spectrum displayed a strong excitation band at 240 nm, in addition to those corresponding to the direct excitation of the Eu^{3+} ground state to higher levels of the 4f-manifold (between 270 and 400 nm),[10a,b] which has been previously attributed to a Eu−O charge transfer transition (CTB) caused by electron delocalization from the filled 2p shell of O^{2-} to the partially filled 4f shell of Eu^{3+}.[11b] As observed in Figure 10, the intensity of the Eu^{3+} emissions was considerably higher when exciting through such CTB band than by direct excitation of the Eu^{3+} electronic levels (λ_{ex} = 395 nm), which should be kept in mind for the optimum performance of these nanophosphors.

Ce^{3+} ions only have one electron in their 4*f* shell, which can be excited to the 5*d* orbitals upon irradiation with UV radiation. The excitation spectrum obtained for our $Ce_{0.05}Y_{0.095}PO_4$ nanophosphor, by monitoring the most intense emission band of Ce^{3+} at 354 nm, consisted of two broad bands in the 230−350 nm region, centered at ~320 and ~252 nm (Figure

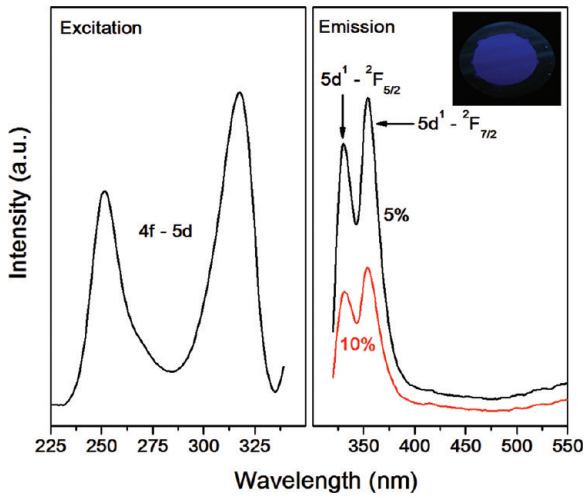

Figure 11. Excitation spectrum (λ_{em} = 354 nm) obtained for the $Ce_{0.05}Y_{0.95}PO_4$ nanophosphor (left) and emission spectra (λ_{ex} = 252 nm) obtained for Ce:YPO_4 nanophosphors having different doping levels (right). Inset: photograph of the $Eu_{0.25}Y_{0.75}PO_4$ phosphor deposited on a Millipore filter, under UV (λ = 254 nm) irradiation.

11) as those previously reported for polycrystalline Ce:YPO_4 (tetragonal) samples.[26] To record the emission spectrum of our nanophosphors, we used the excitation band at lower wavelength (252 nm) for a better observation of all the emission features of the Ce^{3+} ion. As observed in Figure 11, the emission spectra of the two samples displayed two broad bands centered at 330 and 354 nm, corresponding to the transition from the excited $5d^1$ configuration to the $^2F_{5/2}$ and $^2F_{7/2}$ levels of Ce^{3+},[26] which originate a blue (x = 0.150, y = 0.082) (Figure S8, Supporting Information) luminescence (Figure 11, inset). The intensity of such emissions was found to decrease as the Ce content increased from 5 to 10%, clearly manifesting a concentration quenching effect so that the optimum Ce-doped nanophosphor composition corresponded to the formula $Ce_{0.05}Y_{0.095}PO_4$. The luminescence QY for this system could not be measured due to the partial overlapping between the excitation and emission bands (Figure 11).

The excitation spectrum obtained for the $Tb_{0.05}Y_{0.95}PO_4$ nanoparticles, monitored at the most intense Tb^{3+} emission (542 nm)[2b,7c] displayed several bands between 250 and 400 nm (Figure 12), which have been attributed to f−f transitions within the $4f^8$ configuration of Tb^{3+} (in the 300−400 nm region)[27] and to $4f^8$−$4f^75d$ transitions (<300 nm).[2b] In this system, the Tb−O CTB, which must appear at lower wavelength (144 nm), has been shown to be inefficient for Tb^{3+} excitation.[28] The emission spectra obtained for the Tb-doped YPO_4 nanophosphors with different Tb content by exciting at the wavelength of the most intense excitation band (265 nm) are shown in Figure 12. As observed, all spectra showed several bands in the 450−650 nm region, which arise from the $^5D_4$-^7F_j (J = 6, 5, 4, 3) transitions of the Tb^{3+} cations. The green luminescence (x = 0.312, y = 0.542) (Figure S8, Supporting Information) observed for this system (Figure 12, inset) is caused by the most intense emission at 542 nm. Figure 12 also shows that the intensity of the emissions increased as

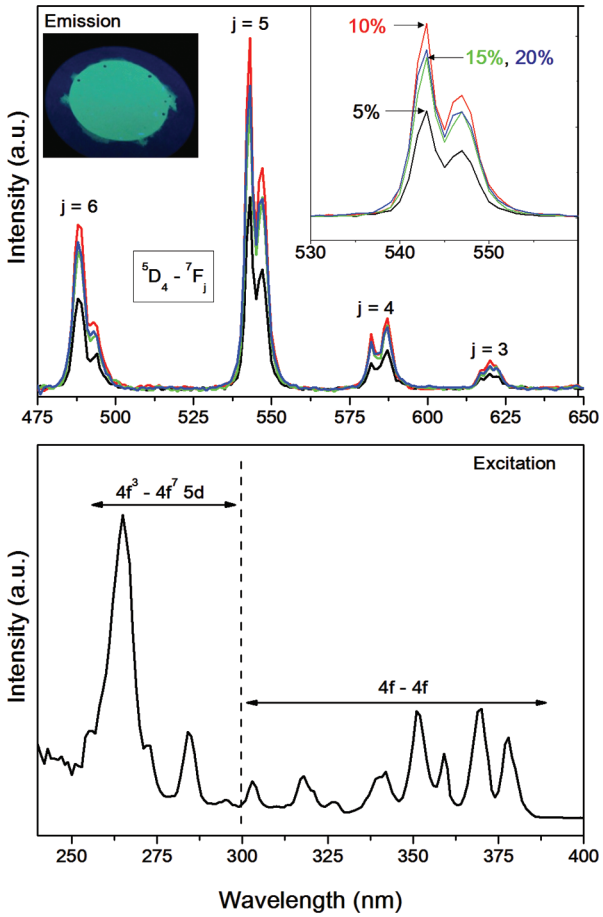

Figure 12. Excitation spectrum (λ_{em} = 542 nm) obtained for the $Tb_{0.05}Y_{0.95}PO_4$ nanophosphor (top) and emission spectra (λ_{ex} = 265 nm) obtained for Tb:YPO_4 nanophosphors having different doping levels (bottom). Insets: enlarged view of the spectra showing the most intense emissions (right) and photograph of the $Tb_{0.10}Y_{0.90}PO_4$ phosphor deposited on a Millipore filter, under UV (λ = 254 nm) irradiation (left).

the Tb content increased from 5 to 10%. However, a further increase of the Tb concentration above 15% gave rise to a decrease of the emissions intensity, manifesting a concentration quenching effect, which was confirmed by the measurement of the luminescence QY of the samples. Thus, the value of this magnitude, which was found to be very high (~80%) for the sample with the lowest doping level ($Tb_{0.05}Y_{0.95}PO_4$), decreased progressively for the more concentrated samples (Table 5). Therefore, the most efficient Tb doped nanophosphor is that with a Tb concentration of 5%. It must be mentioned that because of experimental limitations, the QY measurements were conducted by direct excitation of Tb at the wavelength of its most intense excitation band (351 nm) (Figure 12).

Finally, the excitation spectrum monitored at the main Tb emission line at 542 nm for sample $Ce_{0.05}Tb_{0.05}Y_{0.95}PO_4$ (Figure 13) was quite similar to that of the Ce-doped systems (Figure 11) displaying two broad bands at ~320 and ~252 nm, which confirmed the energy transfer from excited Ce^{3+} to Tb^{3+}.

The emission spectra (Figure 13) obtained for the Ce, Tb codoped nanophosphors by exciting at the most intense excitation band (320 nm) clearly showed the characteristics emissions of Tb^{3+} (from 450 to 650 nm), already observed for the Tb single doped system (Figure 14) along with a much weaker band at 354 nm associated to the Ce ions (Figure 11),

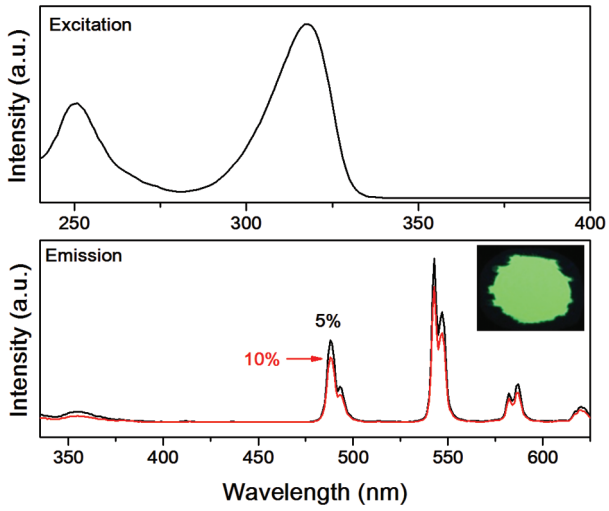

Figure 13. Excitation spectrum (λ_{em} = 542 nm) obtained for the $Ce_{0.05}Tb_{0.05}Y_{0.9}PO_4$ nanophosphor (top) and emission spectra (λ_{ex} = 320 nm) obtained for Ce,Tb:YPO_4 nanophosphors with different doping levels (bottom). Inset: photograph of the $Ce_{0.05}Tb_{0.05}Y_{0.90}PO_4$ phosphor deposited on a Millipore filter, under UV (λ = 254 nm) irradiation.

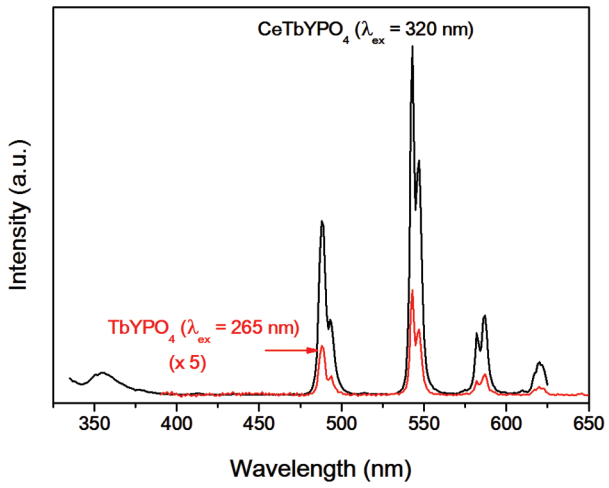

Figure 14. Comparison of the emission spectra obtained for the $Ce_{0.05}Tb_{0.05}Y_{0.9}PO_4$ and the $Tb_{0.05}Y_{0.95}PO_4$ nanophosphors with their optimum λ_{ex}.

which indicated that the energy transfer from the latter to the Tb cations was not complete. Nevertheless, this energy transfer, as expected, gave rise to a remarkable increase of the green (x = 0.315, y = 0.562) (Figure S8, Supporting Information) Tb luminescence (Figure 13, inset and Figure S9, Supporting Information) with respect to the most efficient Tb single doped nanoparticles, as clearly evidenced in Figure 14. Figure 13 also shows that the increase of the Ce content from 5 to 10% in the codoped samples having a Tb^{3+} concentration of 5%, resulted in a small decrease of the emissions intensity as a consequence of a concentration quenching process. Therefore, the most efficient Ce,Tb-doped YPO_4 composition is $Ce_{0.05}Tb_{0.05}Y_{0.95}PO_4$. The QY value obtained for this sample by considering only the Tb emissions was 30% (Table 5), which is close to the average value reported for nanoparticles of the amply studied Ce,Tb:$LaPO_4$ system.[11b,29]

CONCLUSIONS

Mesoporous tetragonal yttrium phosphate nanoparticles with high surface area, variable mean size, narrow size distribution, and lenticular shape can be synthesized by a very simple homogeneous precipitation procedure consisting of aging at low temperature (80−120 °C) ethylene glycol solutions containing only yttrium acetylacetonate and phosphoric acid. The synthesis process is very fast (7 min) and requires the use of a microwave oven for heating. These lenticular nanoparticles are formed through an ordered aggregation of smaller entities, which attach through their crystalline faces parallel to the *c* axis of the tetragonal structure, thus explaining their porosity and high surface area. This synthesis method can be also used to prepare RE-doped YPO_4 nanoparticles (RE = Eu, Ce, Tb, and Ce + Tb) with morphological and structural characteristics similar to those of the undoped system. In all cases, the doping level was optimized resulting in nanophosphors red (Eu), blue (Ce), or green (Tb and Ce + Tb) luminescence with high quantum yields. In particular, for the Eu and Tb doped systems, the optimum nanophosphors presented the highest value of the luminescence quantum yield (60% for Eu and 80% for Tb) so far reported for this kind of nanomaterial. Because of their morphological, microstructural, and luminescent properties as well as because of their dispersibility in water and absence of organic contamination, these nanophosphors are suitable for biomedical application.

ASSOCIATED CONTENT

Supporting Information

TGA curve obtained for the lenticular YPO_4 nanparticles shown in Figure 1 (Figure S1), TEM micrographs of the particles obtained by heating in a conventional oven EG solutions containing 0.02 mol dm^{-3} $Y(acac)_3$ and 0.15 mol dm^{-3} H_3PO_4 for different periods of time (Figure S2), TEM micrographs of the YPO_4 particles obtained by aging a 0.02 mol dm^{-3} $Y(acac)_3$ and 0.15 mol dm^{-3} H_3PO_4 solution in ethylene glycol, at 120 °C for different periods of time (Figure S3), TEM micrographs of RE:YPO_4 nanophosphors (RE = Eu, Tb, Ce, and Ce + Tb) with different doping levels (Figure S4), XRD patterns of Ce-doped YPO_4 nanophosphors with different Ce content (Figure S5), particle size distribution obtained by DLS for the RE:YPO_4 nanophosphors (Figure S6), XRD pattern of the $Ce_{0.15}Tb_{0.05}Y_{0.85}PO_4$ nanophosphor (Figure S7), CIE color coordinates of the RE:YPO_4 nanophosphors (Figure S8), photograph of the $Eu_{0.25}Y_{0.75}PO_4$ and $Ce_{0.05}Tb_{0.05}Y_{0.90}PO_4$ nanophosphors dispersed in water, under UV (λ = 254 nm) irradiation (Figure S9) (PDF). This information is available free of charge via the Internet at http://pubs.acs.org/.

Web-Enhanced Feature

A movie in mpg format showing the full dynamic tomogram is available.

AUTHOR INFORMATION

Corresponding Author

*Phone: +34 954489533. Fax: +34 954460665. E-mail: mjurado@icmse.csic.es.

ACKNOWLEDGMENTS

This work has been supported by Junta de Andalucía (Grants FQM6090, FQM-3994, and FQM3579). S.R.L. wants to thank the Spanish Ministerio de Ciencia y Tecnología for an FPI fellowship. We also thank Dr. Eugenio Cantelar and Dr. Fernando Cussó for their help in the measurements and interpretation of decay curves.

REFERENCES

(1) Riwotzki, K.; Meyssamy, H.; Schanablegger, H.; Kornowski, A.; Haase, M. *Angew. Chem., Int. Ed.* **2001**, *40*, 573.
(2) (a) Rao, R. P. *J. Lumin.* **2005**, *113*, 271. (b) Di, W.; Wang, X.; Chen, B.; Lai, H.; Zhao, X. *Opt. Mater.* **2005**, *27*, 1386.
(3) Guo, N.; Song, Y.; You, H.; Jia, G.; Yang, M.; Liu, K.; Zheng, Y.; Huang, Y.; Zhang, H. *Eur. J. Inorg. Chem.* **2010**, 4636.
(4) Di, W.; Wang, X.; Ren, X. *Nanotechnology* **2010**, *21*, 075709.
(5) (a) Meiser, F.; Cortez, C.; Caruso, F. *Angew. Chem., Int. Ed.* **2004**, *43*, 5954. (b) Zhang, F.; Wong, S. S. *ACS Nano* **2010**, *4*, 99.
(6) Di, W.; Shirahata, N.; Zheng, A.; Sakka, Y. *Nanotechnology* **2010**, *21*, 365501.
(7) (a) Kim, T. W.; Chung, P. W.; Slowing, I. I.; Tsunoda, M. *Nano Lett.* **2008**, *8*, 3724. (b) Liu, J.; Stace-Naughton, A.; Jiang, X.; Brinker, C. J. *J. Am. Chem. Soc.* **2009**, *131*, 1354. (c) Luo, Q.; Shen, S; Lu, G.; Xiao, X.; Mao, D.; Wang, Y. *J. Mater. Chem.* **2009**, *19*, 8079.
(8) (a) Kang, Y. C.; Kim, E. J.; Lee, D. Y.; Park, H. D. *J. Alloys Compd.* **2002**, *347*, 266. (b) Nuñez, N. O.; Liviano, S. R.; Ocaña, M. *J. Colloid Interface Sci.* **2010**, *349*, 484.
(9) (a) Wang, F.; Zhang, Y.; Fan, X.; Wang, M. *J. Mater. Chem.* **2006**, *16*, 1031. (b) Liu, C.; Wang, H.; Li, X.; Chen, D. *J. Mater. Chem.* **2009**, *19*, 3546. (c) Chatterjee, D. K.; Kumara-Gnanasammandhan, M.; Zhang, Y. *Small* **2010**, *6*, 2781.
(10) (a) Nedelc, J. M.; Avignant, D.; Mahiou, R. *Chem. Mater.* **2002**, *14*, 651. (b) Li, C.; Hou, Z.; Zhang, C.; Yang, P.; Li, G.; Xu, Z.; Fan, Y.; Lin, J. *Chem. Mater.* **2009**, *21*, 4598. (c) Wang, F.; Wang, J.; Liu, X. *Angew. Chem., Int. Ed.* **2010**, *49*, 7456. (d) Shan, J.; Uddi, M.; Yao, N.; Ju, Y. *Adv. Funct. Mater.* **2010**, *20*, 3530.
(11) (a) Yan, R.; Sun, X.; Wang, X.; Peng, Q.; Li, Y. *Chem.—Eur. J.* **2005**, *11*, 2183. (b) Mai, H. X.; Zhang, Y. W.; Sun, L. D.; Yan, C. H. *Chem. Mater.* **2007**, *19*, 4514. (c) Huo, Z.; Chen, C.; Chu, D.; Li, H.; Li, Y. *Chem.—Eur. J.* **2007**, *13*, 7714.
(12) (a) Niraj Luwang, M.; Ningthoujam Jagannath, R. S.; Srivastava, S. K.; Vatsa, R. K. *J. Am. Chem. Soc.* **2010**, *132*, 2759. (b) Ray, S.; Banerjee, A.; Pramanik, P. *Mater. Res. Bull.* **2010**, *45*, 870.
(13) (a) Midgley, P. A.; Weyland, M.; Thomas, J. M.; Johnson, B. F. *Chem. Commun.* **2001**, 907. (b) Midgley, P. A.; Ward., E. P. W.; Hungria., A. B.; Thomas, J. M. *Chem. Soc. Rev.* **2007**, *36*, 1477.
(14) Ni, Y. X.; Hughes, J. M.; Mariano, A. N. *Am. Mineral.* **1995**, *80*, 21.
(15) Bernal, S.; Baker, R. T.; Burrows, A.; Calvino, J. J.; Kiely, C. J.; López-Cartes, C.; Pérez-Omil, J. A.; Rodriguez-Izquierdo, J. M. *Surf. Interface Anal.* **2000**, *29*, 411.
(16) Porrès, L.; Holland, A.; Pålsson, L.-O.; Monkman, A.; Kemp, C.; Beeby, A. *J. Fluoresc.* **2006**, *16*, 267.
(17) Matijević, E. *Chem. Mater.* **1993**, *5*, 412.
(18) (a) Nuñez, N. O.; Ocaña, M. *Nanotechnology* **2007**, *18*, 455606. (b) Nuñez, N. O.; Miguez, H; Quintanilla, M.; Cantelar, E.; Cussó, F.; Ocaña, M. *Eur. J. Inorg. Chem.* **2008**, 4517.
(19) (a) Poul, L.; Ammar, S.; Jouini, N.; Fievet, F. *J. Sol-Gel Sci. Tech.* **2003**, *26*, 261. (b) Feldmann, C. *Adv. Funct. Mater.* **2003**, *13*, 101.
(20) (a) Patra, C. R.; Alexandra, G.; Patra, S.; Jacob, D. S.; Gedanken, A.; Landau, A.; Gofer, Y. *New J. Chem.* **2005**, *29*, 733. (b) Zhu, X.; Zhang, Q.; Li, Y.; Wang, H. *J. Mater. Chem.* **2010**, *20*, 1766.
(21) LaMer, V. K.; Dinegar, R. J. *J. Am. Chem. Soc.* **1950**, *72*, 4847.
(22) Di, W.; Zhao, X.; Lu, S.; Wang, X.; Zhao, H. *J. Solid State Chem.* **2007**, *180*, 2478.
(23) (a) Ocaña, M.; Rodríguez-Clemente, R.; Serna, C. J. *Adv. Mater.* **1995**, *7*, 212. (b) Libert, S.; Gorshkov, V.; Goia, D.; Matijevic, E.; Privman, V. *Langmuir* **2003**, *19*, 10679. (c) Zhang, Z.; Sun, H.; Shao, X.; Li, D.; Yu, H.; Han, M. *Adv. Mater.* **2005**, *17*, 42.
(24) Shannon, R. D. *Acta Crystallogr.* **1976**, *A32*, 751.
(25) Inokuti, M.; Hirayama, F. *J. Chem. Phys.* **1965**, *43*, 1978.
(26) Van Pieterson, L.; Reid, M. F.; Wegh, R. T.; Soverna, S.; Meijerink, A. *Phys. Rev. B* **2002**, *65*, 45113.
(27) Di, W.; Wang, X.; Chen, B.; Lü, S. *Mater. Lett.* **2005**, *59*, 2310.

(28) Van Pieterson, L.; Reid, M. F.; Wegh, R. T.; Soverna, S.; Meijerink, A. *Phys. Rev. B* **2002**, *65*, 45114.
(29) (a) Stouwdam, J. W.; Hebbink, G. A.; Huskens, J; van Veggel, F. C. J. M. *Chem. Mater.* **2003**, *15*, 4616. (b) Buissette, V.; Moreau, M.; Gacoin, T.; Boilot, J. P. *Chem. Mater.* **2004**, *16*, 3767. (c) Bühler, G.; Feldmann, C. *Angew. Chem., Int. Ed.* **2006**, *45*, 4864.